ELSEVIER

Journal of Fluids and Structures 26 (2010) 193–204

JOURNAL OF FLUIDS AND STRUCTURES

www.elsevier.com/locate/jfs

The manipulation of trailing-edge vortices for an airfoil in plunging motion

T. Prangemeier, D. Rival*, C. Tropea

Institute of Fluid Mechanics and Aerodynamics, Technische Universität Darmstadt, Darmstadt, Germany

Received 4 February 2009; accepted 14 October 2009
Available online 22 January 2010

Abstract

Trailing-edge vortex manipulation has been investigated using particle image velocimetry (PIV) for an airfoil undergoing harmonic plunging superimposed with a pitching motion near the bottom of the stroke. The so-called *quick-pitch* motion has been evaluated through a comparison with a benchmark pure-sinusoidal plunge motion for $\mathrm{Re} = 30\,000$ and $k = 0.25$. It has been shown that the trailing-edge vortex circulation can be reduced by more than 60% for all quick-pitch cases. The reduction in trailing-edge vortex circulation has been achieved without diminishing the strength of the leading-edge vortex, thus maintaining the lift augmentation achieved through dynamic stall. The improvement over the benchmark case is then confirmed through a statistical analysis. Finally, an analysis of the flow separation over the airfoil shows that the various quick-pitch motions facilitate earlier flow reattachment at the bottom of the stroke.
© 2009 Elsevier Ltd. All rights reserved.

Keywords: Unsteady aerodynamics; Dynamic stall; Trailing-edge vortex

1. Introduction

Insects, birds and bats make use of a range of unsteady aerodynamic effects in order to fly at low Reynolds numbers where the laminar boundary layer is prone to separation, as discussed by Ellington (2006). Complex wing kinematics have been observed for both cruise flight as well as manoeuvering, see Azuma (2006). This study investigates the elimination of certain negative aspects of the dynamic-stall process by careful tuning of the airfoil kinematics. A Reynolds number of $\mathrm{Re} = 30\,000$ and reduced frequency of $k = 0.25$ corresponding to birds and large insects are used here.

Thomas et al. (2004) visualized the flow around free-flying dragonflies demonstrating the existence of large quasi two-dimensional leading-edge vortices (LEVs) over their high aspect ratio forewings. The production of LEVs is a common mechanism used to augment lift in biological flight and has been studied in detail for pitching airfoils. Numerous experimental studies exist, particularly related to helicopter aerodynamics, and have been reviewed in detail by Leishman (2006). Carr et al. (1977) measured the lift, drag and moment coefficients for a pitching airfoil undergoing dynamic stall and found large hysteresis loops that characterize the lift coefficient curve. Lift augmentation was present, as were peaks in drag and negative aerodynamic moment. For a harmonically plunging and pitching foil, Read et al.

*Corresponding author.
E-mail address: rival@mit.edu (D. Rival)

0889-9746/$ - see front matter © 2009 Elsevier Ltd. All rights reserved.
doi:10.1016/j.jfluidstructs.2009.10.003

Nomenclature

A	vortex integration window (m^2)	h_0	plunge amplitude (mm)
α	angle of attack	$h(t)$	plunge position (mm)
α_0	mean angle of attack for pure-plunge	k	reduced frequency, $\pi fc/U_\infty$
α_1	pitch amplitude	v	fluid kinematic viscosity (m^2/s)
$\alpha_{\mathrm{eff}}(t)$	effective angle of attack	ω_z	spanwise vorticity component (s^{-1})
$\alpha_{\mathrm{geo}}(t)$	geometric angle of attack	s	airfoil span (mm)
$\alpha_{\mathrm{plunge}}(t)$	effective angle of attack for pure plunge	Re	Reynolds number, $U_\infty c/v$
c	chord length (mm)	T	cycle period (s)
f	motion frequency (Hz)	t	time (s)
f_{pro}	quick-pitch pronation frequency (Hz)	t_{pause}	duration of pause (s)
f_{sup}	quick-pitch supination frequency (Hz)	t_{pro}	beginning of pronation (s)
Γ	circulation (m^2/s)	$t_{<\mathrm{stall}}$	crossing of static-stall angle (s)
Γ_{TEV}	TEV circulation (m^2/s)	t_{sup}	end of supination (s)
		U_∞	freestream velocity (m/s)

(2003) found instantaneous lift coefficients with values up to 15 and mean lift values over the cycle as high as 5.5. More recently, flow control using active trailing-edge flaps have been examined in the context of helicopter aerodynamics, as demonstrated by Gerontakos and Lee (2008).

For a similar parameter space as studied here, flow visualization of the dynamic-stall process by Panda and Zaman (1994) has shown that not only a LEV but also a trailing-edge vortex (TEV), similar to a starting vortex, is produced for harmonic oscillating airfoils. This TEV is generated through the rolling up of the trailing-edge shear layer as the LEV convects by. Subsequently the vortex pair has been shown to convect downstream to form the so-called *mushroom-wake* structure. Wagner (1925) was the first to describe the negative effects of a starting vortex on lift. Similar to a starting vortex, a TEV is unfavorable to lift as it counteracts the lift-producing circulation (bound vortex). TEV formation is especially detrimental for cyclic motions that produce a TEV on every downstroke, since the relative spacing of the shed vortices to this bound vortex is small. Contrary to the fast convection of a starting vortex, Panda and Zaman (1994) and Rival et al. (2009) have shown that the mushroom-wake structure asymptotically approaches the free-stream velocity, thus countering the bound vortex for a relatively long period of time during the cycle. As previously mentioned, dragonflies periodically produce a LEV on their forewings. However, Thomas et al. (2004) found that no distinct TEV was formed, but rather a shear layer consisting of many smaller TEVs was produced instead. Replacing a large TEV with a shear layer consisting of smaller vortices is beneficial for lift as described by Katz and Plotkin (2001).

When attempting to eliminate the TEV one must consider Kelvin's law:

$$\frac{D\Gamma}{Dt} = 0, \tag{1}$$

which is valid for inviscid, barotropic flows with conservative body forces. In order to satisfy Kelvin's law, the production of both the positive and negative circulation in the flow must be equal to the net lift. Sources of circulation include the bound vortex as well as vortical structures emanating from both leading and trailing edges. During the growth phase of the LEV, counter-rotating vorticity is continually shed from the trailing edge and Kelvin's law is fulfilled. As the LEV passes over the trailing edge, the shear layer rolls up into a distinct vortex. At the same time, vorticity is still produced at the leading edge and the flow around the airfoil develops into a fully separated state. The lingering flow separation after LEV pinch-off does not increase lift but rather the drag, as discussed in Carr et al. (1977), McCroskey (1982) and Leishman (2006).

Ahmed and Chandrasekhara (1994) studied the reattachment process of an oscillating airfoil typical for helicopter applications with a reduced frequency of $k = 0.05$. They found a slow reattachment process with the flow reattaching from front to rear. Separation was maintained until the effective angle of attack fell well below the static-stall angle. Fast flow reattachment not only reduces the size of the force and moment hysteresis, but more specifically the time spent in the disadvantageous low-lift/high-drag regions of the cycle. Green and Galbraith (1995) found that flow reattachment is comprised two overlapping mechanisms. The first is a pitch-rate independent convection wave, which is followed by the pitch-rate dependent re-establishment, a boundary layer and fully attached flow. A more detailed description of the reattachment mechanisms can be found in Sheng et al. (2007). In this study the temporal and spacial resolution does not allow the two mechanisms to be distinguished.

2. Experimental set-up

This study was carried out in the Eiffel-type wind tunnel at the Institute of Fluid Mechanics and Aerodynamics (TU Darmstadt) using the particle image velocimetry (PIV) method; see Fig. 1. A plunging airfoil with a heave amplitude of $h_0/c = 0.5$ was pitched about its quarter-chord position. A carbon-fibre SD7003 wall-spanning profile with a chord length of 120 mm and a span of 450 mm was used. This profile has a static-stall angle of approximately $\alpha = 11^\circ$ at $\mathrm{Re} = 60\,000$, as measured by Selig et al. (1995) and Rival and Tropea (2009), which has been used to characterize the point where the flow reattachment process begins. The use of the static-stall angle to characterize the start of the reattachment process is supported through the experiments of Niven et al. (1989). More details about this low Reynolds number profile, the experimental rig as well as the wind tunnel itself have been presented in detail in Rival et al. (2009).

In Rival and Tropea (2009) both static force measurements and oil visualizations were used to access sting and wall effects. Sting effects were found to be minor and the junction flow was limited to regions within $z = c/8$ of the wall. A recent investigation by Ol et al. (2009) used a very similar strut configuration to drive the same pure-plunge motion as used in this study (reference case). Here three-dimensional effects associated with LEV breakdown were visualized using dye injection. Despite the appearance of three-dimensionality near the bottom of the stroke, there was no evidence linking this phenomenon to the facility boundary conditions. In yet another facility using the same pure-plunge kinematics, see Bansmer et al. (2008), spanwise flows less than 10% of the freestream were measured using PIV. In light of these comparisons with other facilities as well as the strong correlations found on the PIV measurement plane (a maximum of 1% outliers for any given time step), the authors are confident of the bulk two-dimensionality in the flow despite the inherent three-dimensional breakdown of the vortices shed into the wake.

A commercial PIV system was used in this study (Dantec Dynamics A/S) and consisted of a Nd:YAG ($\lambda = 532$ nm) Litron dual-cavity laser with a maximum power output of 135 mJ per cavity and two 10-bit FlowSense 2 M CCD cameras each with a 1600×1200 pix resolution. Due to the large imaging field required, 60 mm $f/2.8$ Nikkor lenses were used. In order to reduce reflections the profile was painted mat-black and monochromatic filters, with a corresponding wavelength of $\lambda = 532$ nm, were installed on the lenses. The laser beam was directed over three mirrors into the test-section and expanded into a sheet approximately 2 mm in thickness. This laser sheet was set parallel to the flow direction and aligned onto the airfoil quarter-span position. Due to the large imaging area of 0.0864 m^2 the laser power was set to 90% for both cavities. With the use of compressed air driven through four Laskin nozzles, DEHS seeding particles less than 1 μm in diameter were introduced into the settling chamber using a vertical rake aligned with the measurement plane.

PIV image pairs were sampled at 15 Hz allowing for six phases to be recorded per cycle at $k = 0.25$. In order to construct the ensemble velocity fields of 12 phases per cycle, two staggered sets with 100 images per phase were

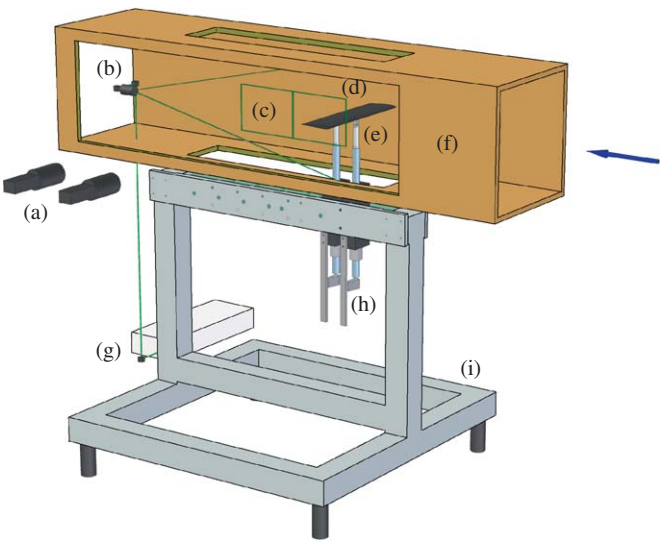

Fig. 1. Experimental set-up in wind tunnel with flow direction from right-to-left: (a) CCD cameras, (b) beam expander, (c) PIV image frames, (d) wall-spanning carbon-fibre profile, (e) embedded piezo-electric force sensors, (f) test-section, (g) laser head, (h) linear motors with linkage system and (i) base structure.

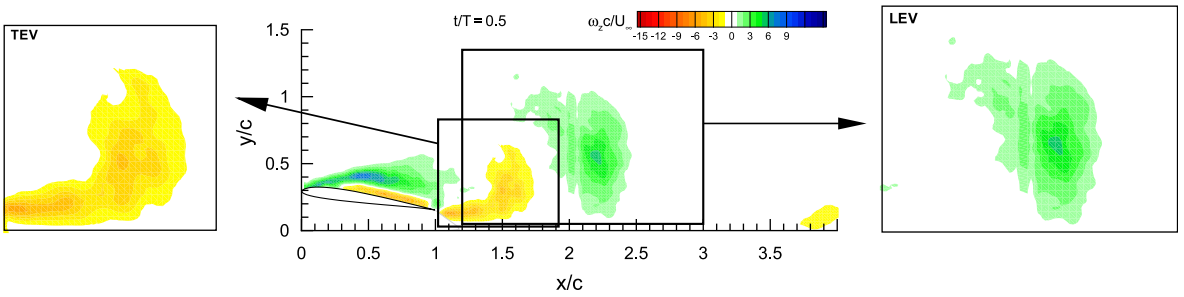

Fig. 2. Dimensionless vorticity plot for the reference case at $t/T=0.5$ showing the windows used to calculate the circulation of the TEV (left) and LEV (right); note no positive vorticity in TEV window and no negative vorticity in LEV window, due to threshold value of zero.

ensemble-averaged. The vorticity was subsequently calculated from these ensemble-averaged vector fields, which had the effect of smoothing the vorticity fields. In all cases the first two starting cycles were removed from all ensembles. Each camera imaged a field corresponding to $x/c=2$ and $y/c=1.5$, with a resolution of 800 pix/c (6.7 pix/mm). Reflections on the model surface were strongest at the bottom of the stroke where a region $0.04c$ normal to the airfoil surface was deemed to be unreliable. Shadows and strong reflections on the pressure (lower) side required masking. Parallax effects were strongest at the top of the stroke and at this position were responsible for hiding a region $0.03c$ normal to the airfoil surface. The vector fields were calculated using an adaptive correlation with 32×32 pix interrogation windows and a 50% overlap. A 3×3 filter was used to lightly smooth the vector fields in order to more clearly define the vortical structures in the wake. A local neighborhood validation using a 9×9 moving-average filter and an acceptance factor of 0.2 was employed to eliminate outliers. This, however, also had the effect of smoothing the velocity gradient and thereby thickening the shear layers. The accuracy of the vector fields was estimated to lie within 2% for all cases. Subsequently the vorticity and circulation could be estimated to have uncertainties of $\Delta\omega c/U_\infty=\pm0.5$ and $\Delta\Gamma/U_\infty c=\pm0.05$, respectively.

The circulation of the vortices was calculated from the local vorticity field using Stokes' theorem via numerical integration:

$$\Gamma=\iint_A \omega_z\,\mathrm{d}A, \tag{2}$$

where A is the window encompassing the vortex in question. The vortices were tracked manually and the vorticity for integration was extracted from their respective windows using a threshold value of zero. As an example, the LEV and TEV windows and their respective positions at bottom dead center for the reference case are presented in Fig. 2.

3. Parameter space

3.1. Kinematics

The reduced frequency was chosen such that a distinct vortical wake was formed for the given amplitude ($h_0/c=0.5$) and mean angle of attack ($\alpha_0=8^\circ$). The appearance of such a distinct mushroom-wake structure in this facility was first observed at $k>0.2$, as reported by Rival and Tropea (2009). A pure-plunge sinusoidal motion used to augment lift has inherent disadvantages, as described by Rival et al. (2009). These include among others the formation of a TEV, which diminishes lift on the airfoil. Another disadvantage is the long recovery period, from $t/T=0.333$ up until the middle of the upstroke, where the region over the airfoil remains separated for a prolonged period of time. While the flow is fully separated, lift drops and the pitch-down moment and drag are increased, see Carr et al. (1977). In order to improve performance, various kinematics such as a so-called *peak-shifted* case have been tested by Rival et al. (2009). While they offer some benefits in terms of LEV formation, more radical alterations of the airfoil kinematics could further improve the performance of the plunging airfoil, specifically by targeting the most disadvantageous aspects of the flow and minimizing them. In this study some of the detrimental aspects of dynamic stall have been reduced by superimposing a quick-pitch motion, which counteracts the TEV and the lingering separation. In Fig. 3 the breakdown of the pure-plunge and quick-pitch motions is presented.

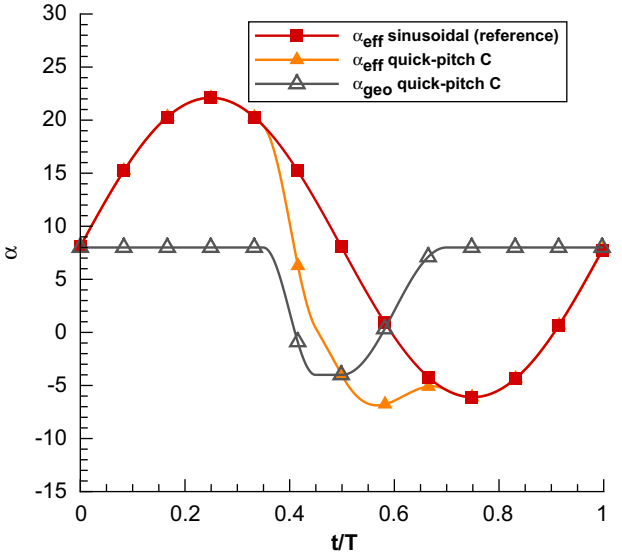

Fig. 3. Individual components of the quick-pitch motion: effective angle of attack (α_{eff}) for the sinusoidal-plunge and quick-pitch cases, geometric angle (α_{geo}) of attack for the quick-pitch case.

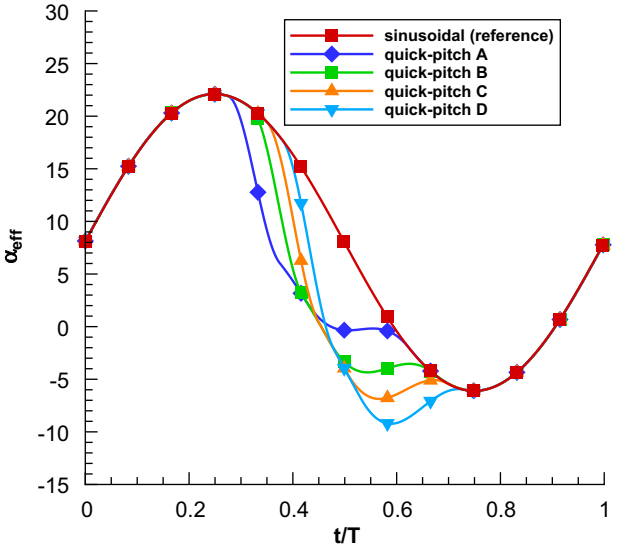

Fig. 4. Effective angle-of-attack distribution for the various quick-pitch cases; note symbols represent the 12 measurement phases over the period.

The effective angle-of-attack distribution as a function of period for all quick-pitch cases is presented in Fig. 4. The quick-pitch kinematics are based upon the sinusoidal motion of the reference case. At a varying time towards the end of the downstroke, a pitch-down motion (pronation) is superimposed onto the reference case. The quick-pitch motion begins by sinusoidally pitching the airfoil down at a frequency five times greater than that of the plunging motion itself. This is followed by a pause in the pitched-down position. Thereafter the airfoil returns to its initial geometric angle of attack at half the rate of the pronation. The timing for the pause and the pitch-up motion were chosen in a way as to maintain as smooth a motion as possible at the bottom-dead-center position, so as to facilitate flow reattachment.

Table 1
Characteristic timing of kinematics and the crossing of the static-stall angle for the various quick-pitch cases.

Case	t_{pro}/T	f_{pro} (Hz)	t_{pause}/T	f_{sup} (Hz)	t_{sup}/T	$t_{<stall}/T$
Reference	–	–	–	–	–	0.476
Quick-pitch A	0.275	12.5	50	6.25	0.625	0.342
Quick-pitch B	0.320	12.5	50	6.25	0.670	0.376
Quick-pitch C	0.350	12.5	50	6.25	0.700	0.398
Quick-pitch D	0.380	12.5	50	6.25	0.730	0.419

The following equation describes the effective angle-of-attack distribution for the pure-plunge motion:

$$\alpha_{plunge}(t) = \alpha_0 + \arctan\left(\frac{2\pi f h_o \sin(2\pi f t)}{U_\infty}\right). \tag{3}$$

As an example Eq. (4) describes the superposition of the quick-pitch motion on top of the pure-plunge motion for the quick-pitch C case:

$$\alpha_{eff}(t) = \begin{cases} \alpha_{plunge}(t) & \text{for } 0 \le t/T < 0.35, \\ \alpha_{plunge}(t)\text{-}\alpha_1(\cos(2n\pi t + \pi) + 1) & \text{for } 0.35 \le t/T < 0.45, \\ \alpha_{plunge}(t)\text{-}\alpha_1 & \text{for } 0.45 \le t/T < 0.5, \\ \alpha_{plunge}(t)\text{-}\alpha_1(\cos(n\pi t + \pi)) & \text{for } 0.5 \le t/T < 0.7, \\ \alpha_{plunge}(t) & \text{for } 0.7 \le t/T < 1. \end{cases} \tag{4}$$

The goal of the quick-pitch kinematics was to specifically target the TEV and the fully separated flow over the airfoil after the LEV has pinched-off. A fast pitching motion is necessary in order to be able to respond to the TEV quickly without affecting the LEV formation process. Furthermore, by pitching down quickly the local effective angle of attack at the trailing edge is reduced (known as dynamic cambering), which further combats the development of the TEV.

The only difference between the various quick-pitch cases is the timing of the beginning of the pitching motion. The pronation (pitch-down) and following supination (pitch-up) are the same for all cases. The timing of the pronation is important as it dictates when the effective angle of attack drops below the static-stall angle, and therefore when production of vorticity at the leading edge is significantly reduced. The timing of the pronation (t_{pro}/T), as well as the resulting timing in crossing back down below the static-stall angle ($t_{<stall}/T$), the end of the supination (t_{sup}/T) and the pause duration (t_{pause}/T), can be found in Table 1.

4. Results

4.1. Vorticity

In this section the vorticity distributions of the quick-pitch cases are compared to that of the reference case, with particular attention being placed on the formation of the TEVs. Presentation of vorticity contour plots is limited to the reference and the quick-pitch A and C cases as these are representative of the three different types of TEVs encountered in this experiment. Fig. 5 shows the dimensionless vorticity contours of the flow field at $t/T = 0.417$ and at $t/T = 0.5$ for the reference, quick-pitch A and C cases. The flow moves from left to right and the airfoil translates downwards until it reaches the bottom-dead-center position at $t/T = 0.5$. Dark regions denote high absolute values of vorticity, whereby the positive (clockwise LEV) and negative (counter-clockwise TEV) regions are separated by white areas of near-zero vorticity. The area underneath the airfoil is masked due to shadows and reflections from the laser light sheet.

First, the reference case without the quick-pitch motion is examined. At $t/T = 0.417$ the LEV has developed and its size is on the order of the chord length. At this phase the LEV passes over the trailing edge and the TEV is formed, as can be seen directly behind the trailing edge in Fig. 5(a). Here the TEV is the most concentrated of all cases. By $t/T = 0.5$ the TEV and LEV have formed the mushroom-wake structure, which then convects downstream. At $t/T = 0.5$ the TEV is found to have grown significantly in size and has convected half a chord length downstream from the trailing-edge, which represents a convection velocity of less than half the free-stream velocity.

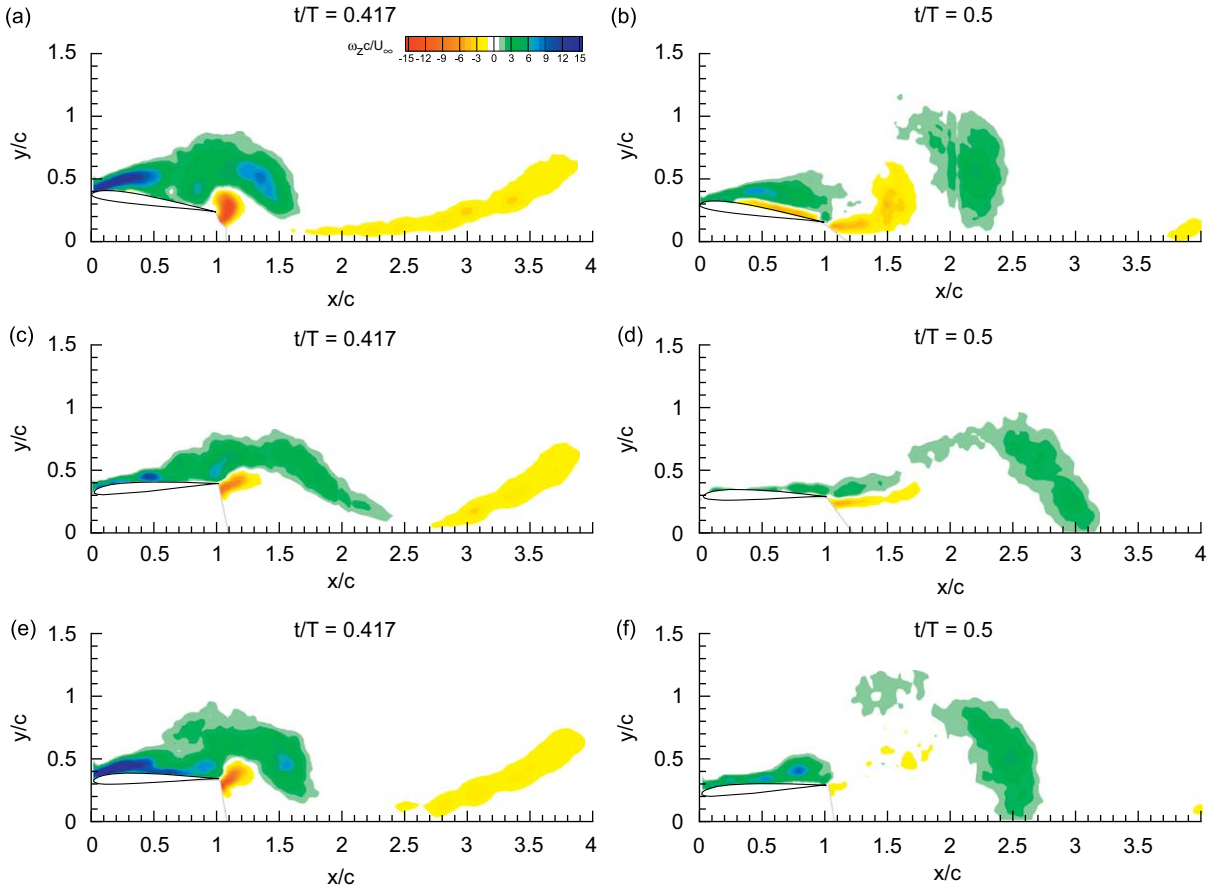

Fig. 5. Plots of dimensionless vorticity showing the TEV formation one phase before bottom dead center ($t/T = 0.417$) and at bottom dead center ($t/T = 0.5$) for the reference (a, b), quick-pitch A (c, d) and quick-pitch C (e, f) cases.

When comparing the TEVs of the quick-pitch and reference cases with one another, major differences become apparent. Unlike the reference case, the airfoil for the quick-pitch A case is in the fully pitched-down position at $t/T = 0.417$. The first significant difference for this case is that the vortex structure at the trailing edge is much more *sheet-like*, reminiscent of a shear layer and less so of the well-defined vortical structure found for the reference case. This is a result of the early pronation, which prevents the formation of the TEV. Major differences between the reference and the quick-pitch C cases have also been identified. The flow field for the quick-pitch C case has similarities with both the reference and quick-pitch A cases. At $t/T = 0.417$ the airfoil is still pronating and a TEV is found at the trailing edge, similar to that of the reference case. In the next time step though, at $t/T = 0.5$, the TEV is significantly dissipated, which can be attributed to the interactions between the vortex and the trailing edge during the pronation.

In order to further understand the TEV development we must also consider the LEV, as the two are invariably linked to one another through Kelvin's law (Eq. (1)). Despite the fact that the bound vortex cannot be measured in this study, a strong correlation between the circulation shed from the leading and trailing edges has been observed in Figs. 5(a), (c) and (e). At $t/T = 0.417$ the reference case has the strongest leading-edge shear layer and therefore also the strongest trailing-edge shear layer. Conversely for the quick-pitch A case, both the weakest leading- and trailing-edge shear layers are found.

The phases where the LEV convects over the airfoil are the most important for lift production. In Fig. 6 the vorticity distribution for the LEV is shown at $t/T = 0.333$ for the various cases. For the reference case the LEV spans from the leading-edge shear layer back towards the trailing edge. A similar vortex is found for the quick-pitch C case, as the airfoil has not yet begun to pronate. For the quick-pitch A case minor differences are observed, which can be attributed to the early pronation of the airfoil. These differences include small structures inside the LEV, as well a downstream shift of the vortex position. Apart from these minor differences, however, the LEV size and strength is by and large the

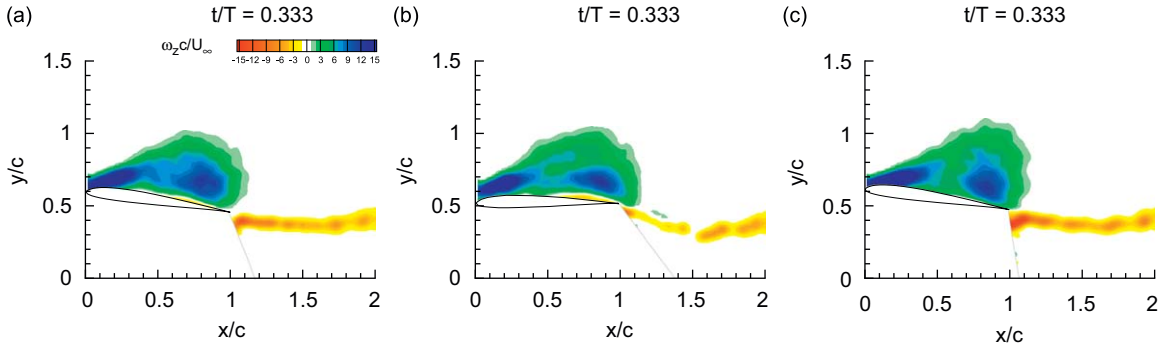

Fig. 6. Plots of dimensionless vorticity showing the LEV formation at $t/T = 0.333$ for (a) the reference, (b) quick-pitch A and (c) quick-pitch C cases.

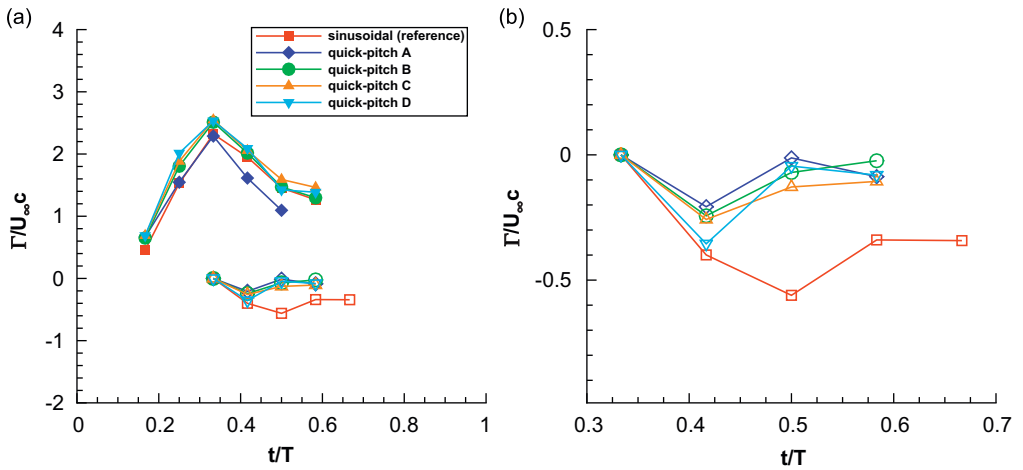

Fig. 7. (a) Development of LEV (solid) and TEV (hollow) circulation as a function of period, and (b) a close-up of the TEV circulation growth.

same as for the reference case. When returning to Fig. 5 one time step later at $t/T = 0.417$, it can be clearly seen that the pronation plays a dominant role on the LEV. However, it is difficult to make any quantitative comparison based on the vorticity distributions alone.

4.2. Circulation

In order to compare the LEV strengths, the dimensionless circulation was calculated from the vorticity field using Stoke's theorem (Eq. (2)). The dimensionless circulation curves for both the LEVs and TEVs are presented in Fig. 7(a) and a close-up of the TEV circulation is presented in Fig. 7(b). It can be seen that for all cases the LEV reaches its maximum strength just before pinching-off from the leading-edge shear layer, as discussed in Rival et al. (2009). The subsequent rapid decrease in out-of-plane vorticity, and therefore circulation, can be attributed to three-dimensional vortex breakdown associated with such massive separations. For the reference case the LEV circulation grows linearly until $t/T = 0.333$ at which point the LEV reaches the trailing edge. In comparison to the reference case, the early pitching case (quick-pitch A) shows a light reduction in the LEV growth rate between the beginning of the quick-pitch motion at $t/T = 0.275$ and the maximum LEV strength at $t/T = 0.333$. Although the pronation begins at $t/T = 0.275$, a return to the static-stall angle is not reached until after the maximum LEV strength is achieved. At $t/T = 0.417$ the LEV convects into the wake and the lift augmentation drops. Therefore a reduction in LEV strength during this latter stage of the downstroke is not so detrimental to performance. Conversely for the late pitching cases (quick-pitch B, C and D), the maximum LEV circulation is somewhat higher. However, the general shapes of these LEV circulation curves are nearly identical to the reference case and are only affected by the state of the boundary layer at the beginning of the

downstroke. An exception to this is the quick-pitch A case, which has a somewhat different shape than the other cases. Its LEV circulation curve shares more similarities with the reference case than with the other quick-pitch cases (B–D), which show effectively no variation amongst themselves. The similarity between these later cases indicates that after approximately $t/T = 0.3$ the dynamic-stall process becomes rather insensitive to the timing of the quick-pitch motion. When examining the LEV circulation development in Fig. 7(a), one can observe that for all quick-pitch cases the LEV begins to form somewhat earlier during the downstroke and reaches a greater maximum value. This variation in LEV formation is attributed to a more quasi-steady boundary layer at the top-dead-center position as a result of earlier flow reattachment during the upstroke. Such history effects have previously been discussed by Rival et al. (2009).

Insight into the reduction of TEV strength can be obtained from the plot of dimensionless circulation in Fig. 7. Circulation is used in order to perform a quantitative comparison of the TEV strength between the reference and quick-pitch cases. When examining the counter-clockwise (negative) circulation in Fig. 7(b), it is evident that for all quick-pitch cases the TEV is significantly diminished. The maximum circulation has moved forward by one phase in all quick-pitch cases from $t/T = 0.5$ to 0.417. Moreover the new maxima in TEV circulation at $t/T = 0.417$ are lower than the corresponding value for the reference case. For the quick-pitch C case it is even less than half the maximum circulation of the reference case. At $t/T = 0.5$ the TEV circulation for all quick-pitch cases is less than a quarter of the peak reference TEV circulation. Table 2 shows the dimensionless TEV circulation values for the relevant phases from $t/T = 0.417$ to 0.583. After summing up the circulation for the three phases when the TEV is present at the trailing edge—where the influence on performance is greatest—it becomes clear that the TEV circulation has been reduced in all cases by at least 60%.

4.3. Statistical analysis of TEV

Since ensemble averaging has the potential of *hiding* vortex structures due to a variation in their position from cycle to cycle, it was deemed prudent to examine the TEVs of each individual cycle separately. In order to ensure that the

Table 2
Dimensionless circulation of the TEV at various points in the cycle.

Case	Reference	Quick-pitch A	Quick-pitch B	Quick-pitch C	quick-pitch D
$t/T = 0.417$	−0.400	−0.206	−0.243	−0.257	−0.354
$t/T = 0.500$	−0.561	−0.001	−0.070	−0.128	−0.045
$t/T = 0.583$	−0.340	−0.087	−0.024	−0.106	−0.081
$\sum$	−1.301	−0.294	−0.337	−0.491	−0.480
%	100%	23%	25%	38%	37%

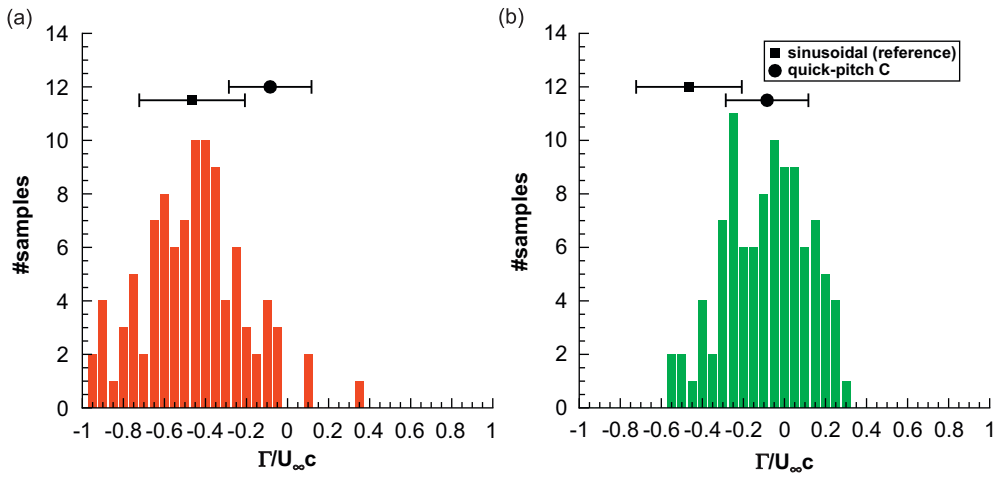

Fig. 8. Histograms of dimensionless circulation for (a) the reference case and (b) the quick-pitch C case; mean and standard deviations for both cases shown above for reference.

differences between the reference and quick-pitch TEVs computed from the ensemble-averaged flow fields are representative of the individual cycles, a statistical analysis of the TEV strength was performed. Instead of calculating the vortex strength from the ensemble-averaged flow field, the circulation was calculated for each of the 100 individual cycles without the use of a threshold. Since many small vortical structures due to the inherent turbulent breakdown are measured, positive values are at times obtained. Histograms of TEV circulation for the reference and quick-pitch C cases at $t/T = 0.5$ are presented in Fig. 8. This time step (at the bottom of the stroke) was selected since it demonstrates the largest variation within the cycle, and offers some insight into the stochastic nature of the vortex breakdown. The mean of the individual TEV circulation and its corresponding standard deviation are shown above the TEV circulation distributions. The mean dimensionless circulation for the reference case is equal to -0.46, which is significantly larger than the value of -0.08 for the quick-pitch C case. Furthermore, the quick-pitch C case is more repeatable than the reference case, as can be seen when comparing their respective standard deviations. Moreover the difference between

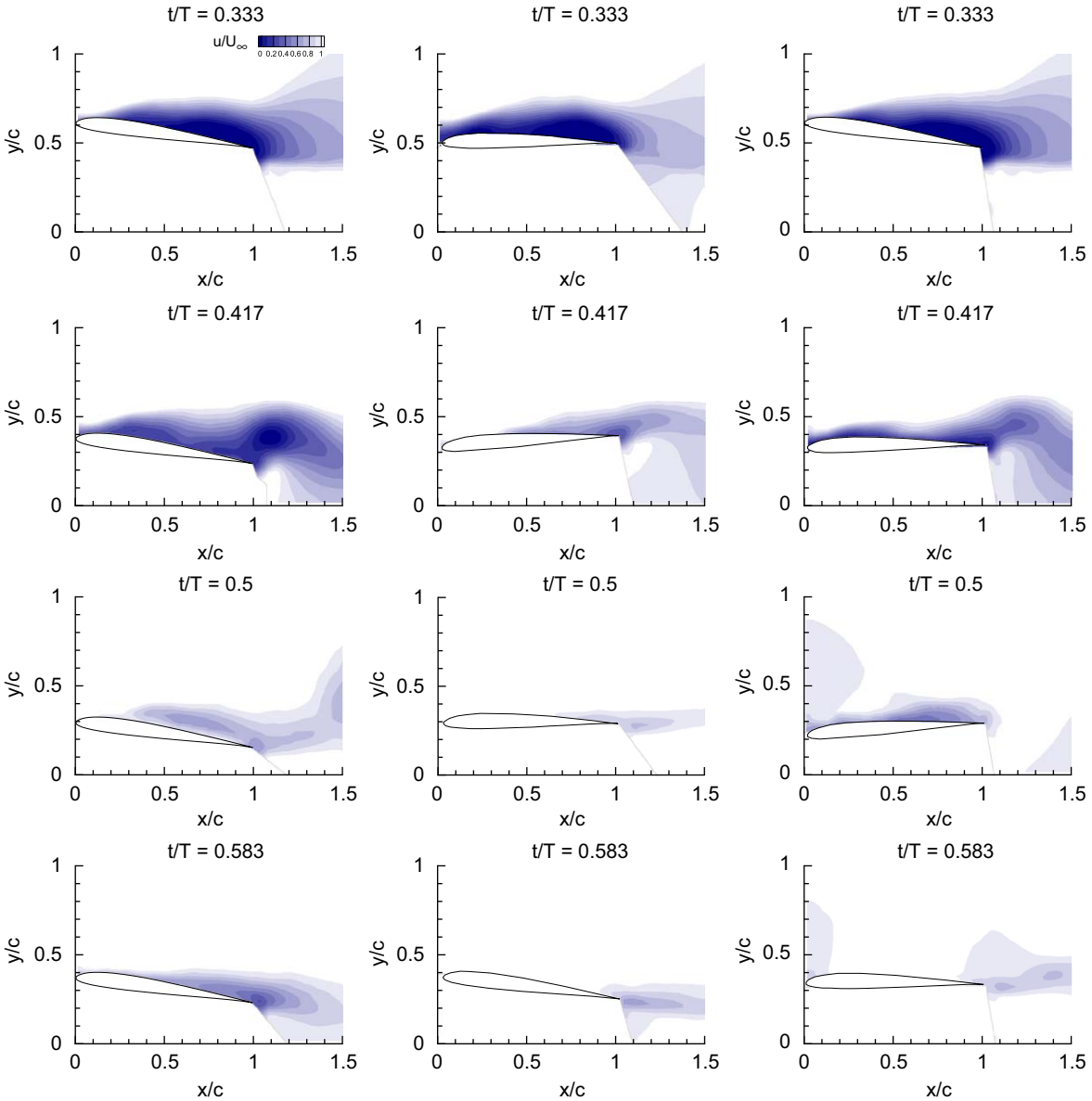

Fig. 9. Contour plots of dimensionless streamwise velocity (u/U_∞) for the phases $t/T = 0.333$, $t/T = 0.417$, $t/T = 0.5$ and $t/T = 0.667$; reference case (left column), quick-pitch A (center column) and quick-pitch C (right column).

the mean circulation of the two cases is larger than the standard deviation of the reference case. Therefore it can be concluded that the ensemble-averaged field is representative of the individual cycles and the reduction in TEV circulation occurs not only for an ensemble-averaged data set but for individual cycles as well.

4.4. Reattachment

In order to gain insight into the reattachment process contour plots of dimensionless streamwise velocity are presented in Fig. 9. For the reference case the separation opens at $t/T = 0.333$ as the outer regions of the LEV reach the trailing edge. After the static-stall angle is crossed, just before the bottom-dead-center position, the flow begins to reattach. At $t/T = 0.5$ and 0.583 the flow at the leading edge of the airfoil is attached and the reattachment process moves towards the trailing edge, culminating in a fully attached flow over the airfoil at $t/T = 0.75$.

The velocity contours for the quick-pitch cases were found to differ from the reference case after sharing a similar stalled condition at $t/T = 0.333$. In particular, the quick-pitch C and reference cases are nearly identical to one another at this point in time. One phase later, at $t/T = 0.417$, the first significant differences in the flow separation become apparent. Here the reference and quick-pitch C cases share a similar saddle shape. In contrast to both these cases, the quick-pitch A case already has flow reattachment at the leading edge. The differences encountered at $t/T = 0.417$ are amplified in the remaining time steps, resulting in attached flow at $t/T = 0.5$ and 0.583 for the quick-pitch cases A and C, respectively. Therefore it can be concluded that the quick-pitch cases achieve attached flow two to three time steps ($0.167 < \Delta t/T < 0.25$) before the reference case. Hence, the duration of the reattachment process is more than one time step shorter for the quick-pitch cases. These differences can be attributed to two effects: the first effect being the timing of the pronation and therefore the crossing of the static-stall angle earlier in the cycle, thus initiating the convective mechanism, and the second effect being the high rate of pitch that accelerates the boundary-layer re-establishment, as demonstrated by Green and Galbraith (1995) and Schreck et al. (1996). In this study, however, the time resolution does not allow for a distinguishment between these two effects on the reattachment process.

5. Conclusions

The manipulation of TEVs for a pitching and plunging airfoil has been investigated using PIV. Various quick-pitch motions were developed and tested in comparison to a pure-plunge reference case, resulting in two distinct flow patterns where the TEV was either reduced in strength or even completely avoided. The latter, represented by quick-pitch A, prevents the formation of a TEV by pitching the airfoil down before the TEV can even begin to form. For the case of TEV circulation reduction, represented by quick-pitch C, the pronation takes place later. Here a TEV begins to form but is quickly dissipated as soon as the airfoil pitches down. All quick-pitch cases demonstrated a reduction of TEV circulation of at least 60%. It has been shown that airfoil kinematics can be used to reduce the negative aspects associated with the dynamic-stall process without infringing upon the lift-augmenting LEV over the airfoil. Flow separation was also investigated and it was found that quick-pitch leads to earlier flow reattachment. This earlier start and shorter duration of the flow reattachment process has the potential to reduce drag and the amount of hysteresis, which can increase the mean lift over the cycle.

Acknowledgments

This research was supported by the Deutsche Forschungsgemeinschaft (DFG) within the national priority program entitled *Nature-Inspired Fluid Mechanics* (SPP1207, Tr 194/40).

References

Ahmed, S., Chandrasekhara, M., 1994. Reattachment studies of an oscillating airfoil dynamic stall flowfield. AIAA Journal 32, 1006–1012.

Azuma, A., 2006. The Biokinetics of Flying and Swimming, second ed. American Institute of Aeronautics and Astronautics Inc, Reston, USA.

Bansmer, S., Scholz, U., Windte, J., Kaehler, C., Radespiel, R., 2008. Flow field measurements on an oscillating airfoil for flapping wing propulsion. In: 46th AIAA Aerospace Sciences Meeting and Exhibit, AIAA 2008-581, Reno, USA.

Carr, L.W., McAlister, K., McCroskey, W., 1977. Analysis of the development of dynamic stall based on oscillating airfoil experiments. NASA Technical Note D-8382.

Ellington, C.P., 2006. Insects versus birds: the great divide. In: 44th AIAA Aerospace Sciences Meeting and Exhibit, AIAA-2006-35, Reno, USA.

Gerontakos, P., Lee, T., 2008. PIV study of flow around unsteady airfoil with dynamic trailing-edge flap deflection. Experiments in Fluids 44, 955–972.

Green, R.B., Galbraith, R.A.M., 1995. Dynamic recovery to fully attached aerofoil flow from deep stall. AIAA Journal 33 (8), 1433–1440.

Katz, J., Plotkin, A., 2001. Low Speed Aerodynamics. Cambridge University Press, Cambridge.

Leishman, J.G., 2006. Principles of Helicopter Aerodynamics, second ed. Cambridge University Press, New York, USA.

McCroskey, W.J., 1982. Unsteady airfoils. Annual Review of Fluid Mechanics 14, 285–311.

Niven, A.J., Galbraith, R.A.M., Herring, D.G.F., 1989. Analysis of reattachment during ramp-down tests. Vertica 13, 187–196.

Ol, M.V., Bernal, L., Kang, C.-K., Shyy, W., 2009. Shallow and deep dynamic stall for flapping low Reynolds number airfoils. Experiments in Fluids 46, 883–901.

Panda, J., Zaman, K.B.M.Q., 1994. Experimental investigation of the flow field on an oscillating airfoil and estimation of lift from wake surveys. Journal of Fluid Mechanics 265, 65–95.

Read, D., Hover, F., Triantafyllou, M., 2003. Forces on oscillating foils for propulsion and maneuvering. Journal of Fluids and Structures 17, 163–183.

Rival, D., Prangemeier, T., Tropea, C., 2009. The influence of airfoil kinematics on the formation of leading-edge vortices in bio-inspired flight. Experiments in Fluids 46, 823–833.

Rival, D., Tropea, C., 2009. Characteristics of pitching and plunging airfoils under dynamic-stall conditions. Journal of Aircraft, in press, doi: 10.2514/1.42528.

Schreck, S.J., Faller, W.E., Luttges, M.W., 1996. Dynamic reattachment on a downward pitching finite wing. Journal of Aircraft 33, 279–285.

Selig, M., Guglielmo, J., Broeren, A., Giguere, P., 1995. Summary of Low-speed Airfoil Data. SoarTech Publications, Virginia Beach, USA.

Sheng, W., Galbraith, R.A.McD., Coton, F.N., 2007. On the return from aerofoil stall during ramp-down pitching motions. Journal of Aircraft 44 (8), 1856–1864.

Thomas, A.L.R., Taylor, G.K., Srygley, R.B., Nudds, R.L., Bomphrey, R.J., 2004. Dragonfly flight: Free-flight and tethered flow visualizations reveal a diverse array of unsteady lift-generating mechanisms, controlled primarily via angle of attack. Journal of Experimental Biology 207, 4299–4323.

Wagner, H., 1925. Über die Entstehung des dynamischen Auftriebes an Tragflügeln. Zeitschrift für Angewandte Mathematik und Mechanik (ZAMM) 5, 17–35.